Comprehensive investigation of three-dimensional diffuse optical tomography with depth compensation algorithm

Haijing Niu
Zi-Jing Lin
Fenghua Tian
Sameer Dhamne
Hanli Liu
University of Texas at Arlington
Department of Bioengineering
Joint Graduate Program between University of Texas at
    Arlington and University of Texas Southwestern Medical
    Center
Arlington, Texas 76019

Abstract. A depth compensation algorithm (DCA) can effectively improve the depth localization of diffuse optical tomography (DOT) by compensating the exponentially decreased sensitivity in the deep tissue. In this study, DCA is investigated based on computer simulations, tissue phantom experiments, and human brain imaging. The simulations show that DCA can largely improve the spatial resolution of DOT in addition to the depth localization, and DCA is also effective for multispectral DOT with a wide range of optical properties in the background tissue. The laboratory phantom experiment demonstrates that DCA can effectively differentiate two embedded objects at different depths in the medium. DCA is further validated by human brain imaging using a finger-tapping task. To our knowledge, this is the first demonstration to show that DCA is capable of accurately localizing cortical activations in the human brain in three dimensions. © *2010 Society of Photo-Optical Instrumentation Engineers.* [DOI: 10.1117/1.3462986]

Keywords: diffuse optical tomography; spatial resolution; depth localization; brain imaging.

1 Introduction

In recent years, the use of near-infrared (NIR) diffuse optical tomography (DOT) has been intensively investigated for non-invasive imaging, such as functional human brain imaging[1,2] and breast cancer detection.[3–5] Several approaches in instrumentation, including continuous-wave (CW), frequency-domain, and time-resolved techniques, have been developed accordingly to face a variety of quantification challenges and broad applications.[6–8] However, the ability to image a deep object remains a challenge for any of the three DOT approaches due to the intrinsic diffuse nature of photons in biological tissues. The high sensitivity of DOT to superficial tissues makes a deep object untruthfully reconstructed toward the surface of the imaging field, leading to a poor depth localization.[9] The cortical activations of the human brain and tumors in the female breast generally occur several centimeters beneath the superficial tissues; thus, they cannot be truthfully localized in depth with using conventional regularized inversion[10] due to the depth-dependent sensitivity of DOT.

Various efforts have been made by several research groups to improve the spatial resolution and depth accuracy of DOT. From the aspect of instrument design, it was experimentally demonstrated that increasing the number of overlapping measurements could improve the spatial resolution of DOT.[9,11] It was also reported that a hybrid image reconstruction method, by combining DOT with prior anatomical information from magnetic resonance imaging (MRI), could overcome the depth limitation of DOT.[12,13] Moreover, it was also proven that an appropriate increase in the source-detector separation within the imaging field improved the depth sensitivity and hence accuracy of the depth localization in DOT.[14] From the aspect of an image reconstruction algorithm, Pogue et al.[15] introduced spatially variant regularization (SVR) to compensate the decrease in measurement sensitivity with increased radial depth, based on the frequency-domain technique and a circular probe geometry that is often used for breast cancer imaging. Culver et al.[16] presented a similar approach for CW-based DOT with reflectance probe geometry for a rat brain model. Both methods modified the penalty term of regularization along depth and thus benefited the image quality of DOT.

Recently, we developed a depth compensation algorithm (DCA), based on maximum singular values (MSVs) of layered sensitivity, to effectively improve the depth localization of DOT in deep tissue.[17] Specifically, the DCA can compensate the severely decreased sensitivity in the deep layers (3 to 4 cm below the surface) by creating a balancing weight matrix that improves the measurement sensitivity with increased depth. This weight matrix is made by inversely arranging MSVs to generate a pseudo-exponential matrix to mandatorily counterbalance the reduced measurement sensitivity in deep layers. With the DCA available, we demonstrated that three-dimensional (3-D) DOT is feasible and can be optimally utilized for functional brain imaging (and other applications). Further understanding of the DCA is needed for its optimal use.

Address all correspondence to: Hanli Liu, PhD, Bioengineering Department, University of Texas at Arlington, Arlington, TX 76019. Tel: 817-272-2054; Fax: 215 272-2251; E-mail: hanli@uta.edu

In this study, we investigated several properties of the DCA in detail, including (1) the depth-dependent sensitivity distribution of the DCA and its comparison to SVR; (2) the dependence of the compensation power, a critical parameter in the DCA, on the optical properties of the background tissue; (3) the improvement of spatial resolution and depth localization of DOT with DCA; (4) an experimental validation of DCA using tissue phantoms with two deep inclusions at different depths; (5) a validation of DCA in 3-D localization of the functional activation of the human brain during a finger-tapping task using simultaneous DOT and functional magnetic resonance imaging (fMRI) measurements; and (6) the extension of the DCA from CW to frequency-domain DOT.

2 Depth Compensation Algorithm (DCA)

2.1 Formation of DCA

This section briefly describes the DCA; a detailed account of this development can be found elsewhere.[17] A weight matrix M can be formed and multiplied to the forward sensitivity matrix A to compensate the exponentially decreased measurement sensitivity in increased depth. Matrix M is defined by

$$M = \{\text{diag}[M(A_l), M(A_{l-1}) \ldots M(A_2), M(A_1)]\}^\gamma, \quad (1)$$

where γ is an adjustable power and varies between 0 and 3, and $M(A_1)$, $M(A_2), \ldots, M(A_{l-1})$, $M(A_l)$ are the maximum singular values for the forward matrix from the first layer to the l'th layer. The multiplication of forward matrix A by M leads to the adjusted matrix $A^\#$ as $A^\# = AM$, which is used in the inverse reconstruction after normalization given by

$$\hat{x} = A^{\#T}(A^\# A^{\#T} + \alpha s_{max}I)^{-1}y, \quad (2)$$

where $\hat{x}$ is the vector of the estimated absorption changes in the image space, y is the vector of measured changes in the optical density from all the source-detector pairs, I is the identity matrix, s_{max} is the maximal singular value of matrix A, and α is the regularization parameter.

A change to the adjustment power γ varies the dynamic strength of weight matrix M, so ultimately the sensitivity distribution for layered voxels in $A^\#$ will be changed. To understand how γ affects the sensitivity distribution of $A^\#$ matrix, we performed computer simulations based on a homogeneous medium whose imaging area on the surface was 8×8 cm^2 with a depth of 5.0 cm, and which had background absorption and reduced scattering coefficients of $\mu_a = 0.08$ cm^{-1} and $\mu'_s = 10$ cm^{-1}, respectively. A κ-square array of 5×5 bifurcated optodes (with a 1.5-cm interval) was arranged on the medium surface. Figures 1(a)–1(g) plot the sensitivity distribution of $A^\#$ in the x-z plane for different γ values, along with their sensitivity profiles at $x=0$ (i.e., along the z direction). Figure 1 shows that when γ was equal to zero (i.e., without any depth compensation), larger sensitivity values were near the superficial layers. When γ was increased from 0.5 to 3, the photon sensitivity of $A^\#$ for superficial layers was forced to decrease, while larger sensitivities were biased toward the deep layers, as shown in Figs. 1(b)–1(g). The adequately enhanced sensitivity to the deep layers led to improved depth localization for a deep object. On the other hand, it is obvious that an inap-
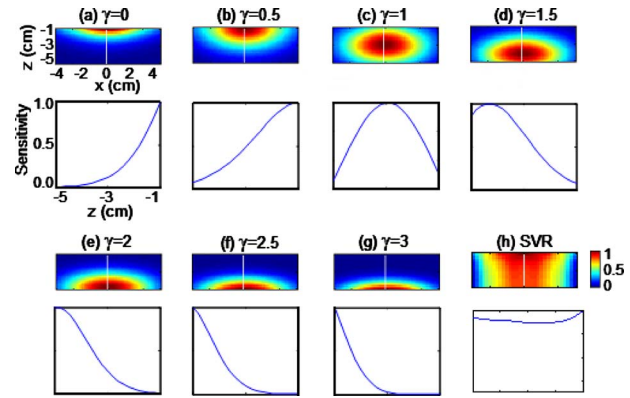

Fig. 1 Sensitivity distributions of $A^\#$ in the x-z plane and their corresponding sensitivity profiles at $x=0$ across the depth below the source location with γ from (a) 0, to (g) 3 in an interval of 0.5 used in the DCA, respectively. (h) Sensitivity distribution obtained with SVR with all the sensitivity maps normalized between 0 and 1.

propriate γ value could cause an overcompensating effect and generate fault reconstructions. The key question is how to determine an optimal γ value.

To answer this question, we performed computer simulations with a 4-mm spherical absorber and $\mu_a = 0.3$ cm^{-1} embedded in a homogeneous medium. The object was moved from $z=-1$ to -5 cm below the measurement surface (i.e., $z=0$) in increments of 0.1 cm. Then we reconstructed the object at each depth using γ values from 0 to 3 with an interval of 0.1. The image quality was evaluated by the contrast-to-noise ratio (CNR)[18] and the positional error (PE), with larger CNR and smaller PE values indicating better quality of a reconstructed image. Figures 2(a) and 2(b) show the computed CNR and PE results as a function of object depth z and adjustment power γ. These figures clearly show that a small, optimal range of γ values between 1.0 and 1.6 (outlined by the dashed boxes) exists for M, providing the best CNR and PE outputs while the object depth varies from $z=-1$ to -5 cm. This observation implies that with an optimal selection of γ, an embedded object in tissue can be reconstructed through DOT with accurate depth localization at both superficial and deep tissue locations.

To further examine if the γ range would be affected by multispectral DOT, such as in cases where the absorption and
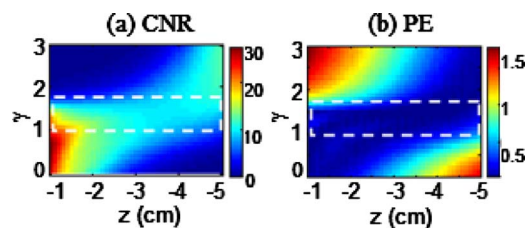

Fig. 2 Dependence of (a) CNR, and (b) PE of reconstructed images on object depth z and γ for an object ($d=4$ mm) located at the center of the x-y plane. These sets of data were generated when simulations moved the object along the z axis from $z=-1$ to -5 cm below the measurement surface ($z=0$), while γ value increased from 0 to 3. The dashed rectangles outline the relatively uniform values of CNR and PE.
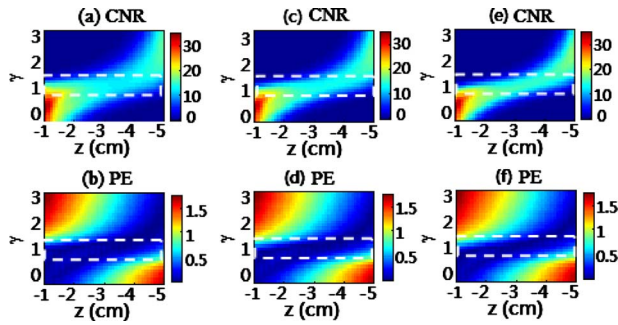
Fig. 3 Dependence of (a) CNR, and (b) PE of reconstructed images on object depth z and γ for an object with absorption coefficient of 0.4 cm^{-1} and 4-mm diameter located at the center of the x-y plane. The background absorption coefficients are 0.1 cm^{-1} for (a) and (b), 0.2 cm^{-1} for (c) and (d), and 0.3 cm^{-1} for (e) and (f). The coefficients were generated when simulations moved the object along the z axis from -1 cm to -5 cm below the measurement surface while the γ value increased from 0 to 3. The dashed rectangles outline the uniform values of CNR and PE.

Fig. 5 Reconstructed $\Delta\mu_a$ images of two absorbers located at $z=-4$ cm with a separation of (a) 1.5 cm, (b) 2 cm, (c) 2.5 cm, and (d) 3 cm. Color bars represent the recovered $\Delta\mu_a$ value, i.e., absorption change. (Color online only.)

scattering coefficients of the background tissue are widely variable at different wavelengths, we performed additional simulations using geometry parameters similar to those used for Fig. 2. The CNR and PE values of the reconstructed images were again used to evaluate image quality. The results are given in Fig. 3 for variable absorption coefficients and Fig. 4 for variable reduced scattering coefficients of the background tissue. Specifically, in Fig. 3 background μ_s' was fixed at 10 cm^{-1} and μ_a values were varied from 0.1 cm^{-1} in Figs. 3(a) and 3(b), to 0.2 cm^{-1} in Figs. 3(c) and 3(d), and to 0.3 cm^{-1} in Figs. 3(e) and 3(f). In Fig. 4, background μ_a was fixed at 0.3 cm^{-1} and μ_s' values were given at 7 cm^{-1} in Figs. 4(a) and 4(b), 10 cm^{-1} in Figs. 4(c) and 4(d), and 15 cm^{-1} in Figs. 4(e) and 4(f). The results clearly show that good image quality, evaluated by both CNR and PE, still held with γ between 1.0 and 1.6. These figures indicate that the γ range between 1.0 and 1.6 was still optimal when the optical properties of the background tissue varied within the biological range. Therefore, we concluded that the DCA was effective even for multispectral DOT, allowing a wide range of optical properties for background tissues.
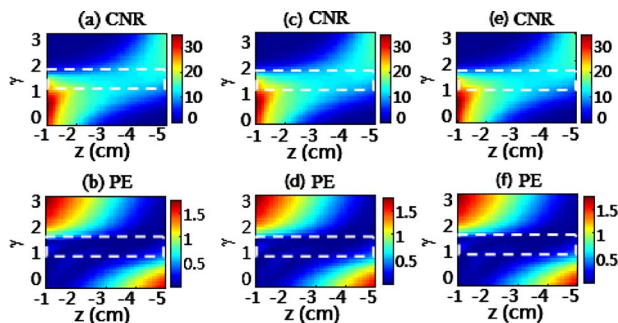

Fig. 4 Simulated parameters are the same as those used in Fig. 3 except that the background scattering coefficients are 7 cm^{-1} for (a) and (b), 10 cm^{-1} for (c) and (d), and 15 cm^{-1} for (e) and (f). The absorption contrast between the inclusion and background is fixed to be 3:1 for all cases.
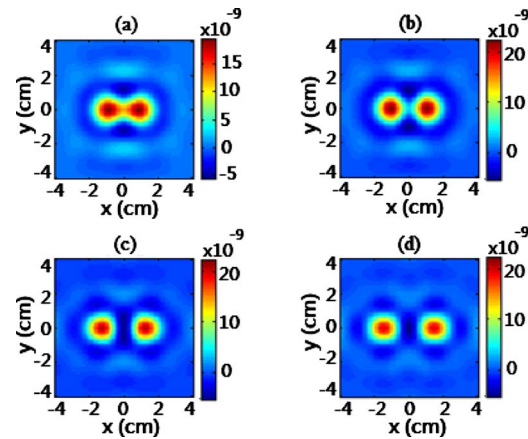
2.2 Spatial Resolution and Depth Localization Studied by Computer Simulations

The spatial resolution and depth localization derived from the DCA were evaluated based on computer simulations using two absorbers with four different separations ($S=1.5$, 2, 2.5, and 3 cm). Similarly, we moved the absorbers from -2 cm to -3 cm to -4 cm in depth to assess the localization accuracy of the DCA. The absorption and reduced scattering coefficients for the absorbers were $\mu_a=0.3$ cm^{-1} and $\mu_s'=10$ cm^{-1}, respectively, giving a 3:1 absorption contrast to the background. The absorbers were 0.6 cm in diameter.

To quantify the performance in spatial resolution, we defined a relative spatial resolution as

$$R = [\hat{x}_{max} - \hat{x}(0)]/(\hat{x}_{max} - \hat{x}_{min}), \qquad (3)$$

where $\hat{x}_{max}=\max(\hat{x})$ and $\hat{x}_{min}=\min(\hat{x})$ are the maximal and minimal values of reconstructed absorption changes in the image space.[19] Therefore, $R=1$ and $R=0$ represent the maximal and minimum spatial resolution, respectively. As an example, Fig. 5 shows lateral reconstructed images of the two inclusions in absorption change (i.e., $\Delta\mu_a$) at $z=-4$ cm, with center-to-center separations of $S=1.5$ cm, 2 cm, 2.5 cm, and 3 cm in Figs. 5(a)–5(d), respectively. The two absorbers with a 1.5-cm separation can still be clearly recognized by using the DCA at a depth of -4 cm ($\gamma=1.3$). For a more quantitative comparison, cross-section profiles of reconstructed $\Delta\mu_a$ values across the two absorbers at $y=0$ (i.e., along the x direction) are plotted in Fig. 6 for each of the three depths and four object separations, with $\gamma=0$ (equivalent to the conventional DOT reconstruction without any compensation) and $\gamma=1.3$, respectively. Correspondingly, the quantification of spatial resolution for each profile of reconstructed $\Delta\mu_a$, based on Eq. (3), are listed in Table 1.

Figures 6(b), 6(d), and 6(f) show that the contrast between the peak and valley values of two objects in the reconstructed x profile was reduced when S was decreased from 3.0 to 1.5 cm, meaning that the spatial resolution was degraded when the DCA was not used. For the objects with
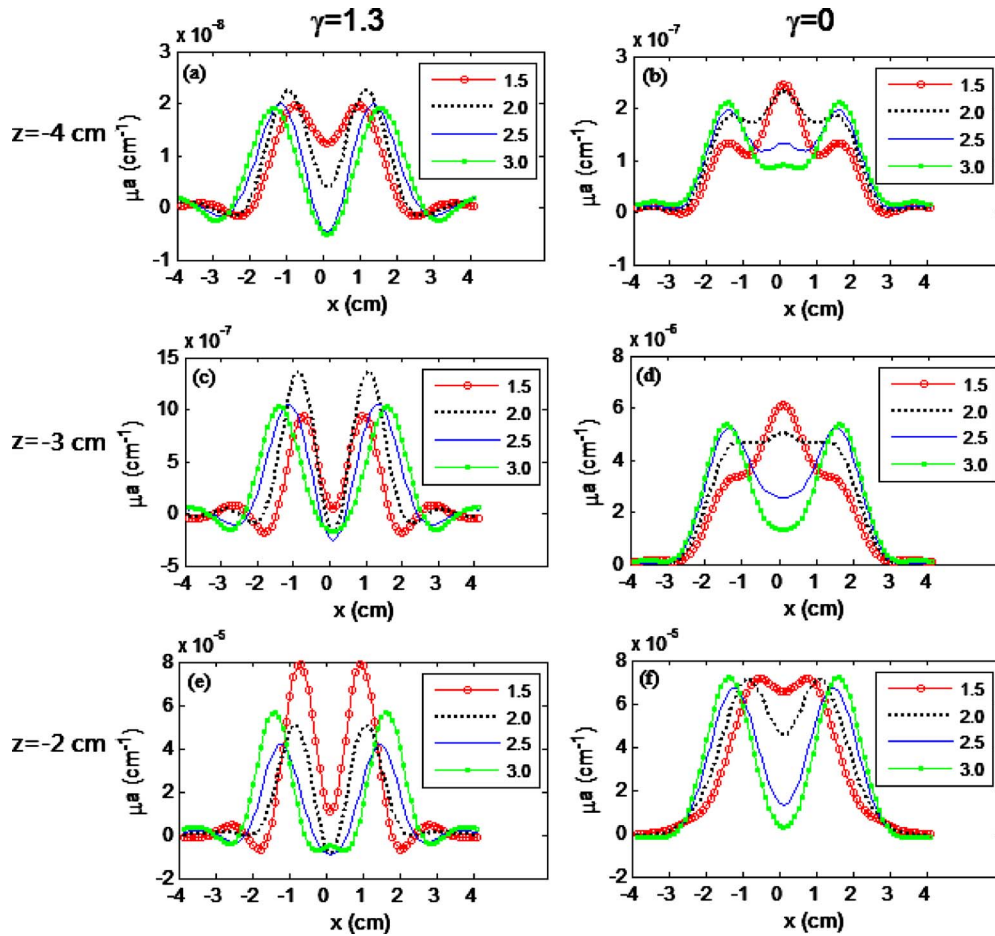
Fig. 6 Profiles of reconstructed $\Delta\mu_a$ values along the x-axis across the two inclusions with variable separations of 1.5 cm, 2.0 cm, 2.5 cm, and 3 cm. The depths of the absorbers are −4 cm [(a) and (b)], −3 cm [(c) and (d)], and −2 cm [(e) and (f)], respectively. The cases of (a), (c), and (e) use $\gamma=1.3$, while (b), (d), and (f) use $\gamma=0$. (Color online only.)

separations of 1.5 cm and 2 cm placed at depths of −3 cm and −4 cm, the quantitative spatial resolution (or the contrast) became zero, as listed in Table 1, thus demonstrating that the objects could not be resolved from the background without using the DCA. On the contrary, Figs. 6(a), 6(c), and 6(e) show that the contrast between the peaks and valleys of the two targets in the reconstructed x profiles remained very distinct while the separation decreased from 3 cm to 1.5 cm at different depths from −2 cm to −4 cm when utilizing the

DCA. All these figures strongly illustrate that the lateral spatial resolution was substantially improved by using the DCA.

Meanwhile, DCA also plays a significant role in improving the accuracy of depth localization. Figure 7 shows DCA-based reconstructed images of two objects placed at different depths (−2 cm to −4 cm) with varying separations (1.5 cm to 2.5 cm). For a quantitative comparison among these images with $\gamma=0$ and $\gamma=1.3$, the positional error for each image is listed in Table 2. The positional errors increased

Table 1 Quantification of spatial resolution R for two reconstructed absorbers with variable separations S located at the three different depths of −2, −3, and −4 cm. The reconstructions were performed using $\gamma=1.3$ and $\gamma=0$, respectively.

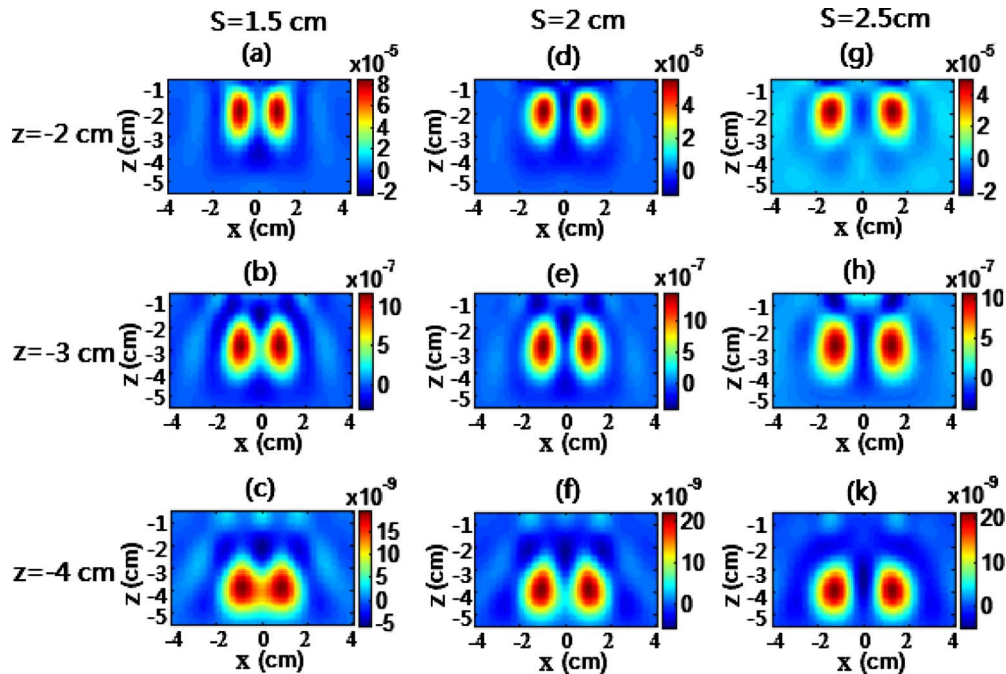|	$\gamma=1.3$				$\gamma=0$			
S (cm)	1.5	2.0	2.5	3.0	1.5	2.0	2.5	3.0
Depth, −2 cm	0.80	1	1	1	0.08	0.37	0.78	0.94
Depth, −3 cm	0.80	1	1	1	0	0	0.51	0.77
Depth, −4 cm	0.65	0.77	1	1	0	0	0.34	0.61

Fig. 7 Reconstructed images of two inclusions in the *x-z* plane for object separations of 1.5 cm [(a), (b) and (c)], 2 cm [(d), (e), and (f)], and 2.5 cm [(g), (h), and (k)] at depths −2 cm [(a), (d), and (g)], −3 cm [(b), (e), and (h)], and −4 cm [(c), (f), and (k)]. Color bars represent the recovered $\Delta\mu_a$ value, i.e., absorption change. (Color online only.)

as the objects were moved deeper into the medium when γ =0. On the other hand, the DCA-based reconstruction with γ=1.3 led to an accurate depth localization for the objects at the superficial or deeper layer, as shown in Fig. 7. Correspondingly, the positional errors were relatively small, regardless of the depth or separation between the two objects. These results again demonstrate that the DCA can greatly improve the depth accuracy in reconstructed images. With the DCA, we were able to resolve two objects placed at a −4-cm depth with a 1.5-cm separation.

3 Validations of DCA by Measurements

To thoroughly validate and demonstrate the performance of the DCA, we first present a tissue phantom study with a challenging experimental setup: two objects located at two differ-

ent depths within a homogeneous medium. Then we validate the DCA by localizing the functional activation in the human brain evoked by a finger-tapping task.

3.1 Phantom Experiments

A multichannel, CW-based, NIR brain imager (DYNOT, NIRx Medical Technologies, LLC, http://www.nirx.net) was utilized to perform the phantom experiment. The imager employed 25 bifurcated fiber bundles in a 5×5 array having a 1.5-cm separation for any given nearest fiber optodes. An Intralipid solution of 1% with μ_a=0.08 cm^{-1} and μ_s' =8.8 cm^{-1} was used to fill a container of 15×10×10 cm^3 as a homogeneous medium. Two spherical absorbers of around 1-cm diameter and μ_a=0.3 cm^{-1} were simultaneously placed at depths of −2 cm and −3 cm below the phantom surface with a center-to-center separation of about 4.1 cm. The probe

Table 2 Positional errors (cm) of the two reconstructed absorbers with variable separations *S* located at the three different depths of −2, −3, and −4 cm. The reconstructions were performed using γ=1.3 and γ=0, respectively.

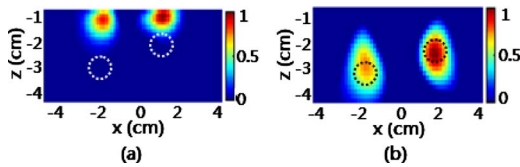|	γ=1.3			γ=0		
S (cm)	1.5	2.0	2.5	1.5	2.0	2.5
Depth, −2 cm	0.03	0	0	0.71	0.72	0.71
Depth, −3 cm	0.11	0.10	0.06	2.69	2.75	2.61
Depth, −4 cm	0.15	0.13	0.09	1.79	1.89	1.63

Fig. 8 Reconstructed DOT images of two objects (dashed circles) placed −2 cm and −3 cm in depth with a center-to-center separation of 4.1 cm in the *x-z* plane. (a) Image formed with $\gamma=0$. (b) Image obtained with $\gamma=1.3$. The color scale is normalized between 0 and 1. (Color online only.)

Fig. 9 Visualization of vitamin E capsules marking the locations of optodes covering the motor cortex of the subject's head in a 3-D view of the fMRI image after 3-D volume rendering.

array was placed on the surface of the liquid phantom. The measured DOT data with and without the absorbers, respectively, were acquired to generate the changes in optical signals seen by all the channels.

Figure 8 shows the reconstructed images of the two inclusions in the *x-z* plane, in which $\gamma=0$ in Fig. 8(a) and $\gamma=1.3$ in Fig. 8(b). Both of these reconstructions provide accurate localizations in the lateral direction along the *x* axis. However, the reconstructed inclusions by $\gamma=0$ are severely biased toward the superficial layers. In particular, the two inclusions are projected wrongly at almost the same depth. On the contrary, the reconstruction with $\gamma=1.3$ shows improved depth accuracy for the two inclusions, and the depth difference between them can be easily observed on top of the background. This laboratory experiment supports the supposition that DCA-based reconstruction with $\gamma=1.3$ can identify not only two inclusions at the correct depth, but also two objects at different depths.

3.2 *Functional Human Brain Imaging in 3-D*

A DOT measurement invoked by finger tapping from a human subject was conducted to validate the depth localization of the DCA by comparing it with the fMRI result. The protocol was approved by the Institutional Review Board at the University of Texas Southwestern Medical Center at Dallas, and the written informed consent was obtained from the subject before the experiment. The fMRI scanning was carried out using a 3-T MR scanner (Siemens Inc., Germany). Functional images were collected axially by using an echo-planar imaging sequence sensitive to blood oxygenation level dependent (BOLD) contrast. The acquisition parameters were as follows: 40 slices, 2000/24 ms (TR/TE, TR means a repetition time and TE means an echo time), 3.2/1.0 mm (thickness/gap), 220×220 mm field of view, 64×64 resolution within slice, and 90-deg flip angle.

To simultaneously acquire the DOT data during fMRI scanning, we utilized a CW-based, fMRI-compatible brain imager (CW5, TechEn) as a data-acquisition system. The probe included four pairs of laser sources (each pair comprised one laser at 690 nm and one at 830 nm) and eight detectors with a 3-cm, nearest-source-detector separation. The data from the nearest source-detector pairs were used to reconstruct the DOT. To co-register the optical probes with respect to the cortex of the subject, vitamin E capsules were positioned on top of each optode/probe. Figure 9 illustrates the positions of the vitamin E capsules in a 3-D MRI structural image of the subject's head obtained after 3-D volume rendering, in which the first and third coronal rows corre-
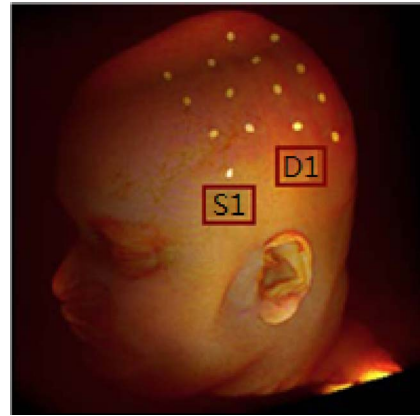
spond to the locations of the light sources and the second and fourth coronal rows correspond to the detectors. These positions helped us to co-register the DOT data with the fMRI results.

In the protocol, the subject was asked to sequentially tap his four fingers together against the thumb of his right hand at a self-paced rate (about 2 to 3 Hz). Visual instructions of the protocol were presented with E-prime software.[20] The protocol was based on a blocked design; within each block, the duration of the finger tapping was 4 s followed by a variable inter-stimulation interval (ISI) of 10 to 16 s to minimize the subject's anticipation of the next coming stimulus. Data collection lasted ~320 s for a total of 16 blocks. Block averaging was used to maximize the signal-to-noise ratio.

Figure 10(a) shows the fMRI images due to functional activation in which the activation was at a depth of nearly 3 cm. Figure 10(b) shows the DOT image of absorption change overlaid on the structural MRI image based on the co-registered landmarks (i.e., the vitamin E capsules) after completion of the image reconstruction based on the DCA with $\gamma=1.3$. The absorption change appears within the cortical region, not in the superficial scalp or skull layer. More importantly, the depth localization from DOT exhibits very good agreement with the fMRI results. Indeed, the DOT results presented here show improved accuracy in depth localization compared with the results reported in Ref. 9, which were based on a cortically constrained technique. This human brain measurement validates the supposition that DCA is an effective method for 3-D DOT to be used for functional brain imaging.

4 Extension of DCA to Frequency-Domain DOT

This section explores the feasibility of applying the DCA to frequency-domain DOT based on computer simulations. In frequency-domain DOT,[21–29] an iterative reconstruction approach is usually adopted to obtain the updated optical parameters using $\hat{X}=J^T(JJ^T+\alpha H_{max}I)^{-1}Y$, where I is the identity matrix; H_{max} is the maximum main diagonal elements of the matrix JJ^T; α is the regularization parameter; and J is the Jacobian matrix for the inverse problem, which maps the
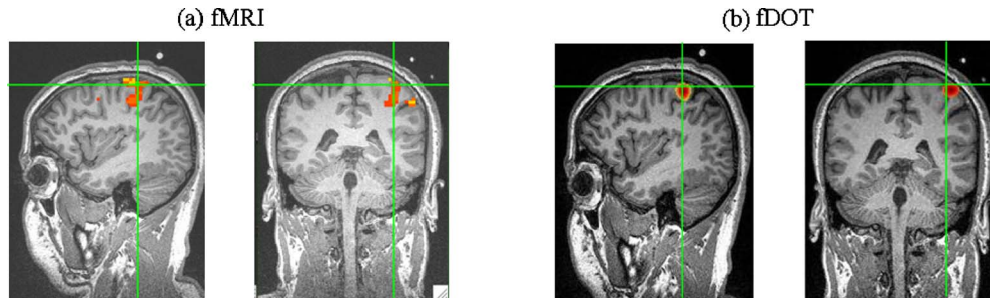
(a) fMRI

(b) fDOT

Fig. 10 (a) fMRI activation images are shown in sagittal and coronal views with 1 to 2 vitamin E capsules shown on the top. The depth of the activated voxels in the motor cortex ranges from 2.5 to 3.5 cm. (b) For illustrative comparison, reconstructed DOT images of motor activation are overlaid on the same brain anatomy obtained by MRI.

changes in log amplitude and phase induced by changes in the absorption and reduced scattering coefficients.[23,25]

The simulated case started with a 2-D 8.6-cm-diameter circular region (to mimic a breast cancer imager); the absorption and reduced scattering coefficients of this region were $\mu_a = 0.1 \text{cm}^{-1}$ and $\mu_s' = 10 \text{cm}^{-1}$, respectively. The 16 sources and 16 detectors were symmetrically arranged around the boundary of the imaging field. This configuration produced a total of 240 amplitude readings and 240 phase readings. A 1-cm circular object was located at the center of the circular field, and the optical coefficients of this inclusion were $\mu_a = 0.2 \text{ cm}^{-1}$ and $\mu_s' = 20 \text{ cm}^{-1}$, providing a 2:1 contrast in both absorption and scattering relative to the background. The iterative procedure was terminated when the difference of the objective function values between two successive iterations was less than 2%, which in the limit can ensure that a stable solution is obtained.[20]

All the nodes with the same radial distance r_j to the center were considered to be within the same layer j. We calculated the maximum singular value for the layered nodes to produce the M matrix, which was multiplied on the amplitude and phase terms of the J matrix to obtain the adjusted matrix $J^\#$. As an example, the sensitivity distributions of matrixes J and $J^\#$ for one source-detector pair are shown in Fig. 11. Figures 11(a)–11(d) are the sensitivity distributions of J before adjustment, and Figs. 11(e)–11(h) are those of $J^\#$ after adjustment. Similar to the CW case, larger sensitivities appear near the sources and detectors at the superficial layers than those in the deep layers when no weight matrix M is multiplied. This attenuated sensitivity distribution will make a reconstructed image that is pulled toward the surface, leading to poor image quality for a deeper object. However, we obtained a compensated sensitivity toward the center field after utilizing the DCA with an appropriate γ value in M. Thus, we anticipate that a centered or deeper object will have improved accuracy in depth localization.

As an example, we ran a simulation with the distribution of μ_a and μ_s', as given in Figs. 12(a) and 12(b). The reconstructed μ_a and μ_s' images without the DCA ($\gamma = 0$) and with the DCA ($\gamma = 1.0$) are shown in Figs. 12(c)–12(f), respectively. Once again, the reconstructed images with the DCA
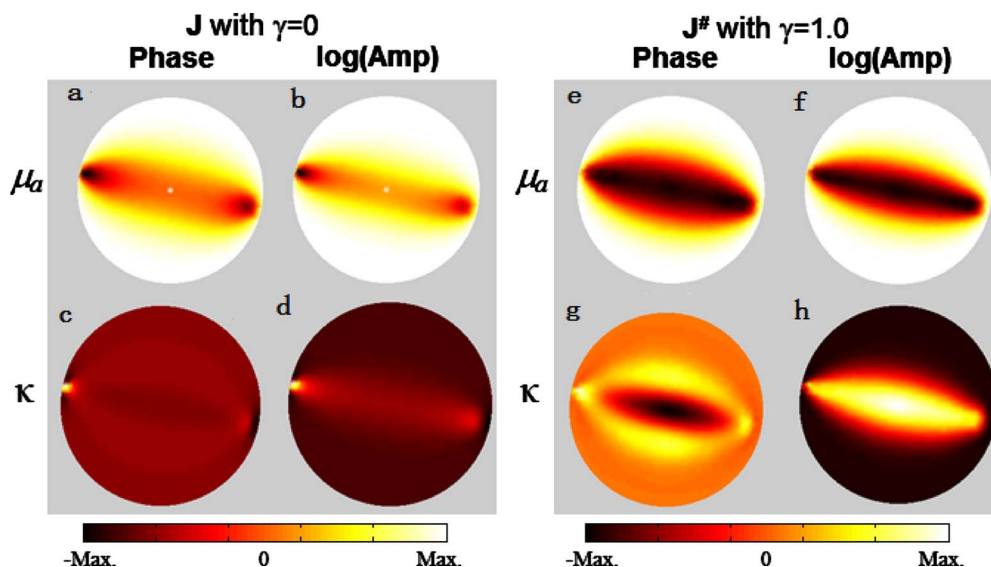

Fig. 11 Initial sensitivity distributions of matrix J in frequency-domain DOT with one S-D measurement: (a)–(d) before using the DCA, and (e)–(h) after using the DCA. (a), (c), (e), and (g): phase sensitivity to μ_a and κ, respectively. (b), (d), (f), and (h): logarithmic amplitude sensitivity to μ_a and κ, respectively.
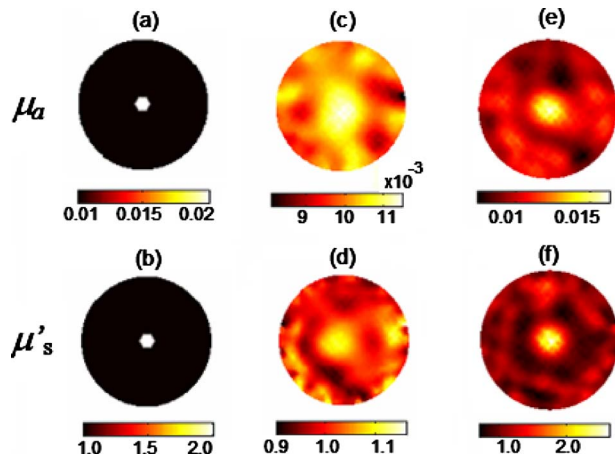
Fig. 12 Original images of (a) μ_a and (b) μ_s' inclusions. Reconstructed (c) μ_a and (d) μ_s' images without the DCA (i.e., $\gamma=0$) and (e) μ_a and (f) μ_s' images with the DCA ($\gamma=1.0$).

show a higher contrast and improved spatial resolution for the inclusion, and have fewer artifacts in the background; the inclusion can be clearly recognized from the background. Thus, through the simulated data, it is clear that the DCA is feasible to be utilized in frequency-domain DOT.

5 Discussion and Conclusions

In this paper, we have described a comprehensive investigation of the DCA. The overall conclusions are (1) the DCA can be used effectively for multispectral DOT imaging with a wide range of μ_a and μ_s' values; (2) the DCA improves both lateral resolution and depth localization in DOT; (3) experimentally, it was clearly shown that the DCA can not only effectively differentiate two embedded objects at different depths, but also reconstruct 3-D DOT for functional human brain imaging; and (4) this depth compensation method can be extended from CW-based DOT to frequency-domain DOT.

Figure 1(a) shows that the adjusted forward matrix $A^{\#}$ degrades back to the original forward matrix A when γ is equal to zero. The sensitivity distribution with unadjusted sensitivity is similar to the distribution of layered MSVs.[30] This consistency forms the basis of the DCA, i.e., the layered MSVs could approximately reflect the decrease of photon sensitivity with increased depth and be used inversely to balance the severe loss in sensitivity. It is also noteworthy that with γ changing from 1.0 to 1.6, larger sensitivities move from superficial layers toward deep layers, leading to optimal imaging quality for the inclusions at different depths. Based on the $A^{\#}$ distribution with an optimal γ value, it is now understood that an improved sensitivity for optimally reconstructed images ought to bias toward a deep layer [for example, Fig. 1(d)], which may explain why the flattened sensitivity distribution apparent in SVR [Fig. 1(h)] would not be able to produce the best image quality for a deep object. In SVR, when the sensitivity distribution is flattened over depth, the depth compensation for deep tissue is not sufficient enough to counterbalance the severe decay in sensitivity; therefore, in SVR the reconstructed images are still pulled toward the surface to

a certain degree. Compared to SVR, the DCA can generate improved image quality for deep objects due to an appropriate compensation power γ.

The physical meaning of γ is that γ represents an equilibrium point that balances the depth-dependent sensitivity decay in matrix A and depth-dependent weight increase in matrix M during image reconstruction. Initially when we studied the adjustable power γ, we empirically chose the range from 0 up to 3 because the sensitivity distribution in deep layers of $A^{\#}$ would achieve a large-enough compensation when $\gamma=3$, as shown in Fig. 1(g). Furthermore, an optimized γ or a small range of γ is determined when it can generate uniform image quality, as quantified by both CNR and PE (Fig. 2) for the same object at variable depths. Indeed, the simulated and experimental results illustrated the validity for this small range of γ.

In this study, the ability of the DCA to accurately locate the depth of deep objects was comprehensively investigated and proven through computer simulations, phantom experiments, and a human brain imaging task. Previous experimental results have shown that the DCA cannot only accurately locate the object depth, but also effectively distinguish two absorbers with an improved spatial resolution.[17] Through this work we wish to convey that the DCA is capable of accurately recovering deeper and smaller-separation objects. However, the DCA has a limited capability to recover the optical properties of the imaged objects because of its empirical nature. Accurate quantification of optical properties has always been a challenge in DOT due to the ill-posed characteristics of inverse problems. Our current effort addresses this issue by developing a new "quantification" algorithm in conjunction with the DCA to improve the reconstruction accuracy of the optical parameters.

In theory, numerical solutions to the diffusion approximation may allow for possible image reconstructions of DOT with a heterogeneous background, but in practice, the ill-posed nature of DOT reconstruction has hampered the studies with a heterogeneous background. At the present time, commonly utilized methods in the DOT field are based on the relatively simple diffusion model with either a semi-infinite, homogeneous condition or a two-layer hemisphere (scalp/skull and brain).[31] The consideration of heterogeneity of the brain is crucial and should be taken into account for DOT image reconstruction as the DOT field advances. This will be the subject of our further study to explore the ability and validity of the DCA for layered structures. Furthermore, biological tissue generally can cover a large range of absorption and scattering coefficients. In this study, by choosing several commonly used optical properties, we wished to show that the optimal gamma range is not greatly altered when the background optical properties are changed.

One weakness of the DCA is that it introduces an adjustable and unknown parameter γ that increases the empirical nature of DOT image reconstruction. In theory, the fewer the empirical parameters used, the more accurate and desirable the DOT images are. In practice, however, it is impossible to generate correct DOT images for deep objects due to the severe decay of measurement sensitivity with increased depth. The addition of one more empirical variable γ, to solve this problem would not create severe errors if the γ is well studied

and understood, and in particular if the variation range of γ is small (between 1 and 1.6). Given the significant improvement in depth localization by the DCA, we believe that its advantages outweigh its disadvantages, while we continue to seek a nonempirical approach. Moreover, since the DCA has an empirically determined parameter γ, it will not generate a significant error in depth localization if the optimal range of γ is varied. While it is true that the uncertainty of γ leads to possible localization errors for the reconstructed object, such errors are in the range of 2 to 3 mm based on our computer simulation results.

References

1. B. W. Zeff, B. R. White, H. Dehghani, B. L. Schlaggar, and J. P. Culver, "Retinotopic mapping of adult human visual cortex with high-density diffuse optical tomography," *Proc. Natl. Acad. Sci. U.S.A.* **104**, 12169–12174 (2007).
2. D. Boas, J. P. Culver, J. Stott, and A. Dunn, "Three dimensional Monte Carlo code for photon migration through complex heterogeneous media including the adult human head," *Opt. Express* **10**, 159–170 (2002).
3. S. Srinivasan, B. W. Pogue, S. Jiang, H. Dehghani, C. Kogel, S. Soho, J. J. Gibson, T. D. Tosteson, S. P. Poplack, and K. D. Paulsen, "Interpreting hemoglobin and water concentration, oxygen saturation, and scattering measured in vivo by near infrared breast tomography," *Proc. Natl. Acad. Sci. U.S.A.* **100**, 12349–12354 (2003).
4. B. W. Pogue, M. Testorf, T. Mcbride, U. L. Osterberg, and K. D. Paulsen, "Instrumentation and design of a frequency-domain diffuse optical tomography imager for breast cancer detection," *Opt. Express* **1**, 391–403 (1997).
5. N. Chen, M. Huang, H. Xia, D. Piao, E. Cronin, and Q. Zhu, "Portable near-infrared diffusive light imager for breast cancer detection," *J. Biomed. Opt.* **9**, 504–510 (2004).
6. J. Selb, A. M. Dale, and D. A. Boas, "Linear 3D reconstruction of time-domain diffuse optical imaging differential data: improved depth localization and lateral resolution," *Opt. Express* **15**, 16400–16412 (2007).
7. J. Wang, B. W. Pogue, S. Jiang, and K. D. Paulsen, "Near-infrared tomography of breast cancer hemoglobin, water, lipid, and scattering using combined frequency domain and cw measurement," *Opt. Lett.* **35**, 82–84 (2010).
8. M. A. Franceschini and D. A. Boas, "Noninvasive measurement of neuronal activity with near-infrared optical imaging," *Neuroimage* **21**, 372—386 (2004).
9. D. A. Boas and A. M. Dale, "Simulation study of magnetic resonance imaging-guided cortically constrained diffuse optical tomography of human brain function," *Appl. Opt.* **44**, 1957–1968 (2005).
10. S. R. Arridge, "Optical tomography in medical imaging," *Inverse Probl.* **15**, R41–R93 (1999).
11. D. A. Boas, K. Chen, D. Grebert, and M. A. Franceschini, "Improving the diffuse optical imaging spatial resolution of the cerebral hemodynamic response to brain activation in humans," *Opt. Lett.* **29**, 1506–1508 (2004).
12. R. L. Barbour, H. L. Graber, J. Chang, S. S. Barbour, P. C. Koo, and R. Aronson, "MRI-guided optical tomography: prospects and computation for a new imaging method," *IEEE Comput. Sci. Eng.* **2**, 63–77 (1995).
13. D. A. Boas, A. M. Dale, and M. A. Franceschini, "Diffuse optical imaging of brain activation: approaches to optimizing image sensitivity, resolution, and accuracy," *Neuroimage* **23**, S275–S288 (2004).
14. E. Okada, M. Firbanj, M. Schweither, S. R. Arridge, M. Cope, and D. T. Delpy, "Theoretical and experimental investigation of near-infrared light propagation in a model of the adult head," *Appl. Opt.* **36**, 21–31 (1997).
15. B. W. Pogue, T. O. McBride, J. Prewitt, U. L. Osterberg, and K. D. Paulsen, "Spatially variant regularization improves diffuse optical tomography," *Appl. Opt.* **38**, 2950–2961 (1999).
16. J. P. Culver, T. Durduran, T. Furuya, C. Cheung, J. H. Greenberg, and A. G. Yodh, "Diffuse optical tomography of cerebral blood flow, oxygen-ation, and metabolism in rat during focal ischemia," *J. Cereb. Blood Flow Metab.* **23**, 911–924 (2003).
17. H. Niu, F. Tian, Z. J. Lin, and H. Liu, "Development of a compensation algorithm for accurate localization of absorber depth in diffuse optical tomography," *Opt. Lett.* **35**, 429–431 (2010).
18. X. M. Song, B. W. Pogue, S. Jiang, M. M. Doyley, and H. Dehghani, "Automated region detection based on the contrast-to-noise ratio in near-infrared tomography," *Appl. Opt.* **43**, 1053–1062 (2004).
19. L. Zhang, F. Gao, H. He, and H. Zhao, "Three-dimensional scheme for time-domain fluorescence molecular tomography based Laplace transforms with noise-robust factors," *Opt. Express* **16**, 7214–7223 (2008).
20. A. Eschman and A. Zuccolotto, *E-Prime User's Guide*, Psychology Software Tools Inc., Pittsburgh (2002).
21. H. Dehghani, B. W. Pogue, S. Jiang, B. Brooksby, and K. D. Paulsen, "Three-dimensional optical tomography resolution in small-object imaging," *Appl. Opt.* **42**, 117–3128 (2003).
22. S. Srinivasan, B. W. Pogue, H. Dehghani, S. Jiang, X. Song, and K. D. Paulsen, "Improved quantification of small objects in near-infrared diffuse optical tomography," *J. Biomed. Opt.* **9**, 1161–1171 (2004).
23. K. D. Paulsen and H. Jiang, "Spatially varying optical property reconstruction using a finite element diffusion equation approximation," *Med. Phys.* **22**, 691–701 (1995).
24. H. Dehghani, B. Brooksby, K. Vishwanath, B. W. Pogue, and K. D. Paulsen, "The effects of internal refractive index variation in near infrared optical tomography: A finite element modeling approach," *Phys. Med. Biol.* **48**, 2713–2727 (2003).
25. H. Jiang, K. D. Paulsen, U. L. Osterberg, B. W. Pogue, and M. S. Patterson, "Optical image reconstruction using frequency-domain data: simulations and experiments," *J. Opt. Soc. Am. A* **13**, 253–266 (1996).
26. H. Niu, P. Guo, L. Ji, Q. Zhao, and T. Jiang, "Improving image quality of diffuse optical tomography with a projection-error-based adaptive regularization method," *Opt. Express* **16**, 12423–12434 (2008).
27. H. Dehghani, B. W. Pogue, S. P. Poplack, and K. D. Paulsen, "Multiwavelength three-dimensional near-infrared tomography of the breast: Initial simulation, phantom, and clinical results," *Appl. Opt.* **42**, 135–145 (2003).
28. H. Xu, H. Dehghani, and B. W. Pogue, "Near-infrared imaging in the small animal brain: optimization of fiber positions," *J. Biomed. Opt.* **8**, 102–110 (2003).
29. X. Song, B. W. Pogue, T. D. Tosteson, T. O. McBride, S. Jiang, and K. D. Paulsen, "Statistical analysis of nonlinearly reconstructed near-infrared tomographic images: Part II—Experimental interpretation," *IEEE Trans. Med. Imaging* **21**, 764–773 (2002).
30. H. Niu, P. Guo, and T. Jiang, "Improving depth resolution of diffuse optical tomography with intelligent method," in *International Conference on Intelligent Computing (ICIC)* **5226**, 514–520 (2008).
31. H. Dehghani, B. R. White, B. W. Zeff, A. Tizzard, and J. P. Culver, "Depth sensitivity and image reconstruction analysis of dense imaging arrays for mapping brain function with diffuse optical tomography," *Appl. Opt.* **48**(10), D137–D143 (2009).